Inverse Primakoff scattering for axionlike particle couplings

C.-P. Wu[,1] C.-P. Liu[,2,3,*] Greeshma C.[,4,5] L. Singh[,4,5] J.-W. Chen[,6,3,†] H.-C. Chi[,2]
M. K. Pandey[,2,6] and H. T. Wong[4,‡]

[1]*Département de Physique, Université de Montréal, Montréal H3C 3J7, Canada*
[2]*Department of Physics, National Dong Hwa University, Shoufeng, Hualien 97401, Taiwan*
[3]*Physics Division, National Center for Theoretical Sciences, National Taiwan University,*
Taipei 10617, Taiwan
[4]*Institute of Physics, Academia Sinica, Taipei 11529, Taiwan*
[5]*Department of Physics, School of Physical and Chemical Sciences, Central University of South Bihar,*
Gaya 824236, India
[6]*Department of Physics, CTP and LeCosPA, National Taiwan University, Taipei 10617, Taiwan*

Axionlike particles (ALPs) can be produced in the Sun and are considered viable candidates for the cosmological dark matter (DM). It can decay into two photons or interact with matter. We identify new inelastic channels of inverse Primakoff processes due to atomic excitation and ionization. Their cross sections are derived by incorporating full electromagnetic fields of atomic charge and current densities, and computed by well-benchmarked atomic many-body methods. Complementing data from the underground XENONnT and surface TEXONO experiments are analyzed. Event rates and sensitivity reaches are evaluated with respect to solar- and DM-ALPs. New parameter space in ALP couplings with the photons versus ALP masses in (1 eV–10 keV) not previously accessible to laboratory experiments are probed and excluded with solar-ALPs. However, at regions where DM-ALPs have already decayed, there would be no ALP-flux and hence, no interactions at the detectors in direct search experiments. No physics constraints can be derived. Future projects would be able to evade the stability bound and open new observable windows in (100 eV–1 MeV) for DM-ALPs.

I. INTRODUCTION

Axions are hypothetical particles first introduced to solve the strong *CP* problem with the spontaneous breaking of the Peccei-Quinn symmetry [1–4]. Theoretical and experimental studies later evolved from the original "QCD axions" to variants generically called "axionlike particles" (ALPs, denoted as *a*), whose masses and coupling strengths with matter are no longer related.

Sources of ALPs are diverse: they are well-motivated dark matter (DM) candidates [5–7] and can be produced in astrophysical environments and terrestrial laboratories. Measurable signatures can be made under a wide variety of experimental techniques [8–15], which include microwave cavities, solar-ALP helioscopes, indirect searches of anomalous electromagnetic radiations in the Universe, as well as production by colliders or strong lasers. Constraints of ALP properties are also derived from cooling of astrophysical objects.

Data from the DM direct search experiments can provide constraints to the ALP-photon coupling $g_{a\gamma\gamma}$ and the ALP-fermion coupling g_{aff}. Through the axioelectric effect, competitive bounds on the ALP-electron coupling g_{aee} have been set in the range of ALP masses 40 eV $< m_a <$ $\mathcal{O}(1 \text{ MeV})$ (natural units with $\hbar = c = 1$ are used throughout this article unless otherwise stated) for DM-ALPs, and in a smaller mass range with solar-ALPs (see Ref. [15]). Laboratory constraints on $g_{a\gamma\gamma}$, however, are comparatively scarce. So far, they are primarily derived from Bragg scattering of solar-ALPs on crystal targets and are only applicable to $m_a < \mathcal{O}(1 \text{ keV})$ [16–20].

The theme of this work is to expand and improve the sensitivities of laboratory experiments in probing the $m_a - g_{a\gamma\gamma}$ parameter space using the inelastic inverse Primakoff (IP) scatterings between ALPs and matter as the detection channels.

This article is structured as follows: theoretical formulation of ALP interactions with matter via $g_{a\gamma\gamma}$-coupling, as well as the evaluation of the corresponding cross sections

*cpliu@mail.ndhu.edu.tw
†jwc@phys.ntu.edu.tw
‡htwong@phys.sinica.edu.tw

are discussed in Sec. II. The observable events on Earth taking solar-ALPs and DM-ALPs as sources are given in Sec. III. Physics results on $g_{a\gamma\gamma}$ by the IP processes from selected laboratory experiments are presented in Sec. IV and are compared with other experimental, astrophysical, and cosmological bounds. It will be shown that new limits are achieved for solar-ALPs. However, the current sensitivity parameter space for DM-ALPs is mostly forbidden for direct detection by the cosmological stability bound, though next generation of experiments would be able to open a new window and study the unexplored parameter space.

II. FORMALISM

The interaction Lagrangian of an ALP field (a) with the photon field (A^μ) and the Standard-Model fermion fields (Ψ_f with f specifying its flavor) is generally written as [14]

$$\mathcal{L}_I = -\frac{g_{a\gamma\gamma}}{4} a F_{\mu\nu}\tilde{F}^{\mu\nu} - \sum_f \frac{g_{aff}}{2m_f}(\partial_\mu a)\bar{\Psi}_f\gamma^\mu\gamma_5\Psi_f, \quad (1)$$

where $F^{\mu\nu} = \partial^\mu A^\nu - \partial^\nu A^\mu$ and $\tilde{F}^{\mu\nu} \equiv \frac{1}{2}\epsilon^{\mu\nu\rho\sigma}F_{\rho\sigma}$ are the photon field tensor and its dual, with $\epsilon^{0123} = 1$; m_f is the fermion mass; and $g_{a\gamma\gamma}$ (g_{aff}) denotes the strength of the ALP-photon (ALP-fermion) coupling. These interaction terms provide the foundation for ALP detection and production. In this work, we will focus only on the processes resulting from a finite $g_{a\gamma\gamma}$.

The coupling $g_{a\gamma\gamma}$ can manifest experimentally in many ways as shown in Fig. 1. The most straightforward channel is where an ALP can have two-photon decay (TPD) in vacuum,
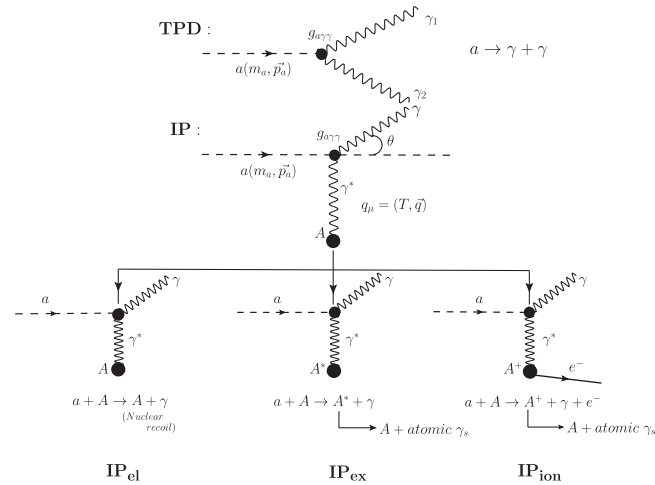

FIG. 1. Schematic diagrams of ALP two-photons decay in vacuum (TPD) and the three IP scattering channels in matter, where kinematics allows one of the photons to be virtual.

$$a \to \gamma_1 + \gamma_2: \quad \Gamma_{a\gamma\gamma}^V = \frac{1}{64\pi}g_{a\gamma\gamma}^2 m_a^3, \quad (2)$$

where $\Gamma_{a\gamma\gamma}^V$ is the decay rate at rest per ALP. When one of the photons becomes virtual in a medium and is absorbed by the target atom A, it gives rise to IP scattering [21–28] with four-momentum transfer $q_\mu \equiv (T, \vec{q})$. There are three IP reaction channels: $a + A \to$

$$\begin{cases} \gamma + A & \text{IP}_{el}: \text{ elastic scattering} \\ \gamma + A^* & \text{IP}_{ex}: \text{ atomic excitation} \\ \gamma + A^+ + e^- & \text{IP}_{ion}: \text{ atomic ionization.} \end{cases} \quad (3)$$

All four channels involve full conversion of the ALPs so that the experimental measurable is the total energy E_a. There is no interference among them, since all have experimentally distinguishable final states—two γ's for TPD, a single γ for IP$_{el}$, a γ plus atomic deexcitation photons for IP$_{ex}$, and a γ plus an ionized electron with atomic transition photons for IP$_{ion}$. At m_a much lower than the nucleus mass scales (GeV), the energy depositions at detectors are electromagnetic without complications of nuclear recoil.

A. Differential cross sections and rates

Evaluation of the double differential cross sections of the ALP IP processes builds on our earlier work of incorporating the atomic many-body physics effects to low energy neutrino [29–31] and DM [32,33] interactions with matter,

$$\frac{d\sigma_{\text{IP}}}{dTd\Omega} = \frac{\alpha g_{a\gamma\gamma}^2}{16\pi}\left(\frac{E_a - T}{v_a E_a}\right)\left[\frac{V_L}{(q^2)^2}\mathscr{R}_L + \frac{V_T}{(Q^2)^2}\mathscr{R}_T\right], \quad (4)$$

where α is the fine structure constant, v_a is the ALP velocity, q^2 and $Q^2 = T^2 - q^2$ are the three- and four-momentum transfer squared, respectively. The kinematic factors V_L and V_T will be given in Eqs. (7) and (8), respectively. The full unpolarized atomic response consists of the longitudinal and transverse components, $\mathscr{R}_L$ and $\mathscr{R}_T$, both being functions of T and q^2 given by

$$\mathscr{R}_{L,T} = \sum_F \overline{\sum_I} |\langle F|\rho, \vec{j}_\perp|I\rangle|^2 \delta(E_I - E_F - T), \quad (5)$$

which arise from the charge ρ and transverse current density $\vec{j}_\perp$, respectively. Note that the longitudinal current density is effectively included in the former by current conservation and also manifested in the change of the photon propagator from $1/Q^2$ to $1/q^2$. The initial state $|I\rangle$ corresponds to the ground state of the target atom, while the choice of final state $|F\rangle$ depends on the IP interaction channels: the ground, excited and continuum states for IP$_{el}$, IP$_{ex}$, and IP$_{ion}$, respectively. In general, the transverse response is less than the longitudinal response by a factor of $\sim\alpha$ since the atomic

current density is suppressed relative to the atomic charge density by the electron velocity.

Experimentally, the observables are the energy of the IP photon (E_γ) and the energy transferred (T) to the scattered atom as atomic recoil, excitation, or ionization. The differential rate recorded by a detector is with respect to the total observable energy E_a of the ALP, which is the sum of E_γ and T. The double differential rate is with respect to E_γ and T simultaneously, where more elaborated analyses are necessary to correlate these two signals. We focus in this work the simplest one: a single differential rate with respect to E_a,

$$\frac{dR_{\mathrm{IP}}}{dE_a} = N_A \sigma_{\mathrm{IP}}(E_a) \frac{d\phi}{dE_a}, \qquad (6)$$

where N_A is the total number of target atoms, $\sigma_{\mathrm{IP}}(E_a)$ and $d\phi/dE_a$ are the total IP cross section [a double integration of Eq. (4)], and energy spectrum of ALPs with incident energy E_a, respectively.

B. Regularization of divergences

To fully exhibit the pole structure of the photon propagator, which is crucial in cross section calculations, the corresponding kinematic factors V_L and V_T are cast in powers of q^2 and Q^2,

$$V_L = 2[E_a^2 - m_a^2 + (E_a - T)^2]q^2 - (q^2)^2$$
$$- (T^2 - 2E_aT + m_a^2)^2, \qquad (7)$$

$$V_T = m_a^4 + \frac{Q^2}{2q^2}[(m_a^4 - 4m_a^2 E_a T)$$
$$+ (2m_a^2 + 4E_a^2 - 4E_aT + 2T^2)Q^2 - (Q^2)^2]. \qquad (8)$$

The familiar Coulomb pole $q^2 = 0$ is realized in the longitudinal component only at the forward angle $\theta = 0$ along with the condition $T = E_a(1 - v_a)$. Since the last term of Eq. (7) vanishes identically as $q^2 \to 0$, only a single pole in $V_L/(q^2)^2$ is produced. This divergence is usually regulated by Coulomb screening in media (see, for example, Refs. [22,23,26,27,34]) via changing the longitudinal propagator from $1/q^2$ to $1/(q^2 + \Lambda_L^2)$. The cutoff Λ_L, which is medium dependent, modifies the infinite-range Coulomb interaction to a Yukawa one with a range of order $1/\Lambda_L$, typically $\sim$Å. We note that this procedure only applies to electrons that are not localized, for example, valence electrons in semiconductors. For a single atom, its neutrality automatically screens its Coulomb field. A manifestation of this fact is the response $\mathscr{R}_L$ starts at the order of $(q^2)^2$, as demonstrated in Eq. (10) and Table 1 of Ref. [28]. [The $\mathscr{R}_L$ responses for IP_ex and IP_ion also start at the order of $(q^2)^2$, but they are due to wave function orthogonality.] Furthermore, the inner shell electrons
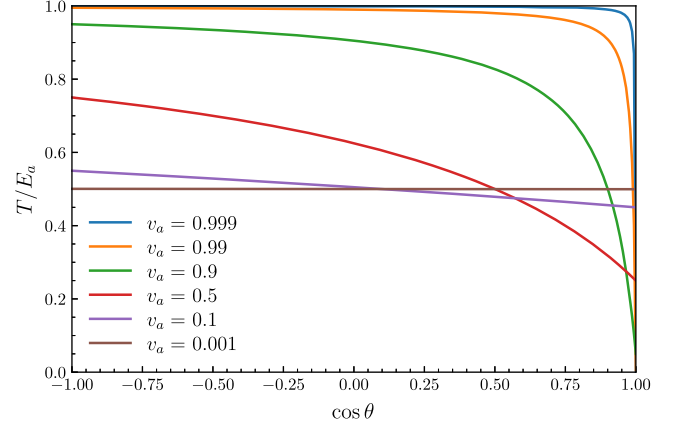

FIG. 2. Contours of $Q^2 = 0$ in the IP processes traced by the ALP scattering angle $\cos\theta$ and fraction of energy transfer (T/E_a) for selected values of v_a.

experience and contribute to screening at shorter length scales than the size of an atom. As a result, applying a universal screening length $\sim$Å tends to overestimate the atomic Coulomb field. This is the main reason that previous calculations using $\sim$Å screening lengths overpredicted IP_el cross sections by solar-ALPs, as was first pointed out and corrected through realistic atomic calculations in Ref. [28].

The transverse component $V_T/(Q^2)^2$ does exhibit a double pole structure at $Q^2 = 0$ for nonzero m_a.[1] The kinematics of the incoming ALP and outgoing photon makes it possible to have

$$Q^2 = m_a^2 - 2E_a(E_a - T)(1 - v_a \cos\theta), \qquad (9)$$

vary from timelike to spacelike as the scattering angle (θ) increases. Figure 2 depicts the $Q^2 = 0$ contours traced by $\cos\theta$ and the fraction of energy transfer (T/E_a) at selected v_a. For ultrarelativistic (UR) ALPs with $v_a \approx 1$, such as solar-ALPs, the divergence only happens at the forward angle. As v_a becomes less relativistic, the timelike to spacelike transition happens at some intermediate scattering angle. For nonrelativistic (NR) DM-ALPs with $v_a \sim 10^{-3}$ (where $E_a \approx m_a$), the pole is realized at a tiny range around $T \approx m_a/2$. As the virtual photon is absorbed by the target, the kinematics of the final state of the target further limits the available Q^2 space. In general, Q^2 can be both spacelike and timelike for IP_ex and IP_ion, while $Q^2 \leq 0$ for IP_el.

To regulate the transverse photon pole, at which the virtual photon approaches the real limit, we follow the approach of Ref. [35] and modify the photon propagator according to the complex refractive index of the detector

---

[1]Note that the $1/q^2$ factor in V_T does not yield a pole, as the numerator that follows also vanishes identically with $Q^2 = T^2$ when $q^2 \to 0$.

material: $\tilde{n} = n_r + in_i$, where the real part n_r gives the normal refractive index, and the imaginary part is related to the attenuation coefficient $\Lambda_T = 2Tn_i$. If the detector consists of only one type of atom with a number density n_A and photoabsorption cross section $\sigma_\gamma(T)$, we can further relate $\Lambda_T = n_A\sigma_\gamma(T)$. As a result, the photon propagator in vacuum should be modified to be

$$\frac{1}{Q^2} = \frac{1}{T^2 - q^2} \rightarrow \frac{1}{T^2\tilde{n}^2 - q^2}$$
$$\rightarrow \frac{1}{(Q^2 - \frac{1}{4}\Lambda_T^2) + T^2(n_r^2 - 1) + iT\Lambda_T}. \quad (10)$$

For simplicity, we take $n_r = 1$ in this paper, which is a good approximation for x-ray and γ-ray photons, and leave refined treatments for photons of lower or near-resonance energies for future studies. The square of the propagator in Eq. (4), which itself is an absolute value squared, becomes

$$\frac{1}{(Q^2)^2} \rightarrow \frac{1}{(Q^2 - \Lambda_T^2/4)^2 + T^2\Lambda_T^2}. \quad (11)$$

Typical values are $n_A \sim 10^{22}/\mathrm{cm}^2$, and $\sigma_\gamma(T) \lesssim 10^6$ barn for $T > 100$ eV. As a result, Λ_T is not larger than a few eV, so the shift in the pole position is not significant, and $T\Lambda_T$ is within the range 10^2–10^4 eV^2. We note that the above treatment requires the virtual photon to be absorbed inside the detector, or equivalently the length dimension of the detector has to be substantially bigger than the attenuation length $1/\Lambda_T$.

C. Equivalent photon approximation

To acquire further insight into the transverse contribution, it is useful to perform an equivalent photon approximation (EPA), similar to the method adopted in Ref. [35], by (i) setting $V_L = 0$, (ii) keeping the sole m_a^4-term in V_T, and (iii) substituting the transverse response $\mathscr{R}_T(T, q)$ by photoabsorption cross section—$\mathscr{R}_T(T, q) \approx T\sigma_\gamma(T)/(2\pi^2\alpha)$. The single differential cross section (SDCS) for IP$_{\mathrm{ion}}$ can then be easily integrated to give

$$\frac{d\sigma}{dT}\Big|_{\mathrm{IP_{ion}}}^{\mathrm{EPA}} = \frac{g_{a\gamma\gamma}^2}{32\pi^2}\left(\frac{\sigma_\gamma}{\Lambda_T}\right)\left(\frac{m_a^4}{v_a^2 E_a^2}\right)$$
$$\times \tan^{-1}\left[\frac{Q^2 - \Lambda_T^2/4}{T\Lambda_T}\right]\Big|_{Q_{\min}^2}^{Q_{\max}^2}. \quad (12)$$

Several important features can be observed: First, the $1/\Lambda_T$ dependence clearly traces the divergence resulting from the double pole. Together with σ_γ, it leads to a single-atom cross section suppressed by $1/n_A$, due to the fact that the effective interaction range becomes shorter as the medium gets denser. Second, the factor $m_a^4/(v_a^2 E_a^2) = m_a^2(1 - v_a^2)/v_a^2$ indicates that this contribution favors NR ALPs with a big mass.

Moreover, when both $Q_{\max}^2$ and $-Q_{\min}^2$ are much larger than $T\Lambda_T$, the arc-tangent value saturates to π. As a result, the SDCS becomes a T-independent constant as long as the kinematics allows Q^2 to change sign when the scattering angle increases. For highly NR cases with $v_a \ll 1$, this requires T in the range of $m_a(1 \pm v_a)/2$, and, as an approximation, the total cross section can be easily integrated to be

$$\sigma_{\mathrm{IP_{ion}},\mathrm{NR}}^{\mathrm{EPA}} \approx \frac{g_{a\gamma\gamma}^2}{32\pi}\left(\frac{1}{n_A}\right)\left(\frac{m_a^3}{v_a}\right). \quad (13)$$

Considering a detector of volume V (the number of atoms is thus $n_A V$) and an ALP number density of n_a (the flux is thus $n_a v_a$), the event rate will be

$$R_{\mathrm{IP_{ion}},\mathrm{NR}}^{\mathrm{EPA}} \approx \frac{g_{a\gamma\gamma}^2}{32\pi}m_a^3(n_a V) = 2\Gamma_{a\gamma\gamma}^V(n_a V). \quad (14)$$

Note that $n_a V$ is the total number of ALP inside the detector volume, so this result gives the total IP$_{\mathrm{ion}}$ event rate twice as much as the two-photon decay (time dilation is negligible because $v_a \ll 1$). The factor of 2 can be understood in the context of EPA that either of the decayed photons can play the role of the intermediate state in the IP process. This result might seem surprising as the predicted rate only depends on a detector volume but not on the target characteristics. However, one should be alert that this approximation is only valid when all the underlying assumptions hold true. For instance, if ALP is not extremely NR, or when the transverse contribution is subdominant, the cross sections and rates have to be explicitly computed. We will discuss this in more detail through concrete cases in the next section.
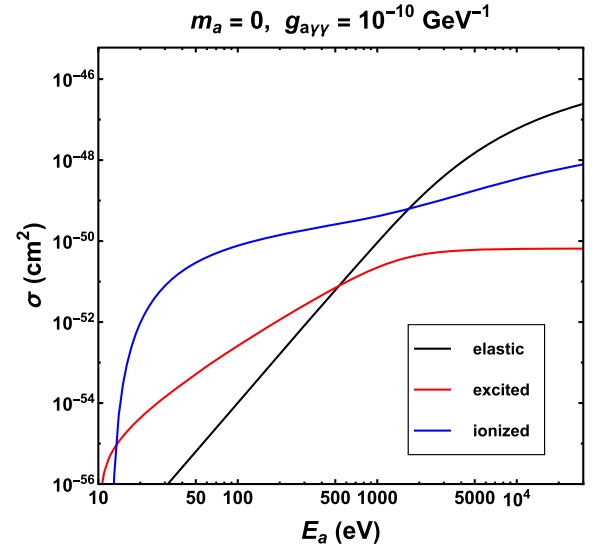

FIG. 3. Total cross sections for the three IP detection channels for the case of a massless ALP scattering off a xenon atom with $g_{a\gamma\gamma} = 10^{-10}$ GeV^{-1}.

D. Selected numerical results

In this subsection, we present numerical results using xenon as the target and assuming $g_{a\gamma\gamma} = 10^{-10}$ GeV^{-1}, to illustrate several key kinematic features when ALPs are either UR or NR.

The scattering cross sections for a massless ALP as a function of E_a are displayed in Fig. 3, where the black, red, and blue curves denote the IP_{el}, IP_{ex}, and IP_{ion} channels, respectively. At high energy where $E_a \gtrsim 2$ keV, IP_{el} dominates the total cross section. On the other hand, IP_{ion} provides the leading contribution at $E_a < 1$ keV, where IP_{el} is suppressed due to the large electronic screening in the charge form factor.

Several special cases of massive ALPs are shown in Figs. 4(a) and 4(b) for IP_{el} and IP_{ion}, respectively. In IP_{el}, Q^2 can only be spacelike. As illustrated in Fig. 4(a), the total cross section is mostly due to the longitudinal response and approaches the massless limit whenever the ALPs become relativistic. Conversely, the cross section drops quickly to zero near energy thresholds due to the NR suppression of $V_L \propto q^2$ and the vanishing of phase space. On the other hand, Fig. 4(b) indicates that the contributions from IP_{ion} are complicated by the enhancement of the double pole in Q^2, which is associated with the transverse response and is proportional to $m_a^2 (1 - v_a^2)^2 / v_a^2$. The departures from the massless case are more dramatic near the energy thresholds, and also grow with the mass.

(a)

Elastic: $g_{a\gamma\gamma} = 10^{-10}$ **GeV**$^{-1}$
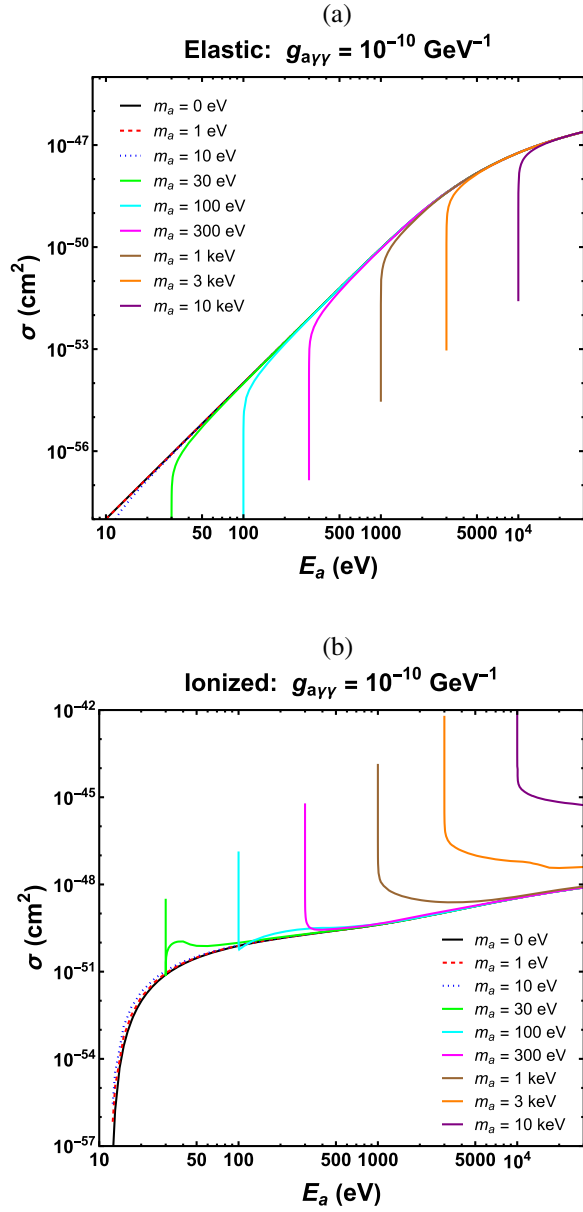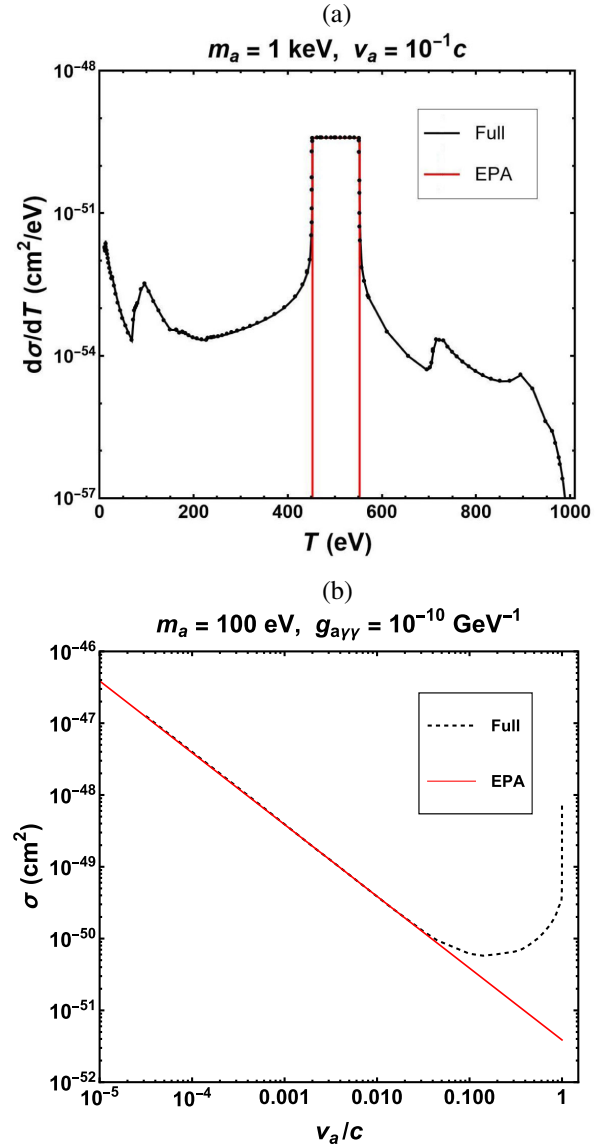

(b)

Ionized: $g_{a\gamma\gamma} = 10^{-10}$ **GeV**$^{-1}$

FIG. 4. Total cross sections for massive ALPs scattering off a xenon atom in the (a) elastic IP_{el} and (b) ionization IP_{ion} channels, at $g_{a\gamma\gamma} = 10^{-10}$ GeV^{-1}.

(a)

$m_a = 1$ **keV,** $v_a = 10^{-1}c$

(b)

$m_a = 100$ **eV,** $g_{a\gamma\gamma} = 10^{-10}$ **GeV**$^{-1}$

FIG. 5. Comparison between the full calculation and EPA for the IP_{ion} process in xenon: (a) the differential cross section with $m_a = 1$ keV and (b) total cross section with $m_a = 100$ eV, with $g_{a\gamma\gamma} = 10^{-10}$ GeV^{-1} in both cases.

The IP$_\text{ion}$ SDCS for an NR ALP with $v_a = 0.1$ and $m_a = 1$ keV is presented in Fig. 5(a). The full calculation (in black), which is based on the atomic wave functions obtained by the frozen core approximation (FCA) and numerical integration of Eq. (4), is compared with the EPA (in red) as prescribed by Eq. (13). In the energy range where the double pole can be accessed (450–550 keV), the EPA is indeed an excellent approximation. Outside this region, where there are contributions from the longitudinal and other transverse responses, the corrections to the total cross section are at the $\sim 1\%$ level. Figure 5(b) shows the total IP$_\text{ion}$ cross section for ALP at $m_a = 100$ eV as a function of v_a. The EPA works well in the NR regime of $v_a \lesssim 0.05$. As v_a approaches the relativistic limit, contributions from the longitudinal responses gradually take over and become dominant.

III. SOURCE-SPECIFIC EVENT RATES

Two ALP sources are considered in this work: one from the Sun, and the other under the assumption that all the galactic dark matter are ALPs.

A. Solar-ALPs

The Sun can produce ALPs through both $g_{a\gamma\gamma}$ and g_{aee} processes. Since only detection channels involving $g_{a\gamma\gamma}$ are considered in this work, we take only the solar-ALP flux generated through the Primakoff process [36]. The resulting detectable event rate is consequently proportional to $g_{a\gamma\gamma}^4$.

With the Primakoff process, thermal photons in the solar interior are converted into ALPs in the Coulomb fields of nuclei and electrons in the solar plasma. The recoil effect is ignored, and the axion energy E_a is identical to the photon energy. The conversion rate is given by [37]

$$
\begin{aligned}
\Gamma_{\gamma \to a} = \frac{g_{a\gamma\gamma}^2 \mathrm{T}_p \kappa^2}{32\pi} & \left[\frac{(m_a^2 - \kappa^2)^2 + 4 E_a^2 \kappa^2}{4 E_a p_a \kappa^2} \right. \\
& \times \ln \left(\frac{(E_a + p_a)^2 + \kappa^2}{(E_a - p_a)^2 + \kappa^2} \right) \\
& \left. - \frac{m_a^4}{4 E_a p_a \kappa^2} \ln \left(\frac{(E_a + p_a)^2}{(E_a - p_a)^2} \right) - 1 \right], \quad (15)
\end{aligned}
$$

where p_a is the ALP momentum. In the UR case where $p_a \approx E_a$, the formula can be simplified to a more popular form [38],

$$
\Gamma_{\gamma \to a}^{\text{UR}} = \frac{g_{a\gamma\gamma}^2 \mathrm{T}_p \kappa^2}{32\pi} \left[\left(1 + \frac{\kappa^2}{4 E_a^2} \right) \ln \left(1 + \frac{4 E_a^2}{\kappa^2} \right) - 1 \right], \quad (16)
$$

where T_p is the plasma temperature, and κ is the Debye screening scale given by [39]

$$
\kappa^2 = \frac{4\pi\alpha}{T} \left(n_e^{\text{eff}} + \sum_j Z_j^2 n_j^{\text{eff}} \right), \quad (17)
$$

with n_e^{eff} and n_j^{eff} are, respectively, the effective number density of electrons and ions with nuclear charge Z_j. The approximate effective electron number density can be expressed as

$$
n_e^{\text{eff}} \simeq \frac{(X+1)}{2} \left(\frac{\rho}{m_u} \right), \quad (18)
$$

where X is the hydrogen mass fraction, ρ is the mass density, and m_u is the atomic mass unit (approximately the proton mass).

The differential flux of solar-ALPs on Earth can be written as

$$
\frac{d\phi_a}{dE_a} = \frac{1}{\pi^2 d_\odot^2} \int_0^{R_\odot} dr \Gamma_{\gamma \to a} \left[\frac{r^2 E_a^2}{e^{E_a/T_p} - 1} \right], \quad (19)
$$

where $R_\odot$ is the solar radius, $d_\odot = 1.5 \times 10^{13}$ cm is the distance to the Sun, and the integration is with respect to the radial distance from the solar center (r). In order to perform the integration, we adopted the BS05-AGSOP solar model [40] for the radial profiles of T_p and κ. The solar-ALP spectra thus derived are depicted in Fig. 6.

Once the solar-ALP spectra ($d\phi_a/dE_a$) are derived, the event rates of the three IP channels can be evaluated directly by Eq. (6). However, in the derivation of the TPD rate, it is important to take the time dilation factor into account since most solar-ALPs are relativistic, so that the TPD rate,

$$
\frac{dR_{\text{TPD}}}{dE_a} = (\gamma^{-1} \Gamma_{a\gamma\gamma}^V) \left(\frac{V}{v_a} \right) \frac{d\phi_a}{dE_a}, \quad (20)
$$

carries an additional correction factor of $\gamma^{-1} = m_a/E_a$ to the decay rate at rest.

1. Solar-ALPs at sub-keV mass (ultrarelativistic)

As displayed in Fig. 6, the typical energy of solar-ALP is in the range of a few to tens of keV. Therefore, ALPs produced in the Sun with sub-keV mass are mostly relativistic and, as explained in Sec. II D, the atomic longitudinal response dominates the IP processes. The differential rates expected at a liquid xenon detector with a ton-year exposure for the four observation channels at $g_{a\gamma\gamma} = 10^{-10}$ GeV^{-1} and $m_a = 0.1$ keV are displayed in Fig. 7(a). The gross feature of the three IP channels is consistent with Figs. 3 and 4—in the entire keV range, the IP$_\text{el}$ has the largest count rates except when $E_a \lesssim 2$ keV, where IP$_\text{ion}$ starts to play an important role. On the contrary, IP$_\text{ex}$ does not contribute significantly, and TPD is also suppressed by the time dilation factor.
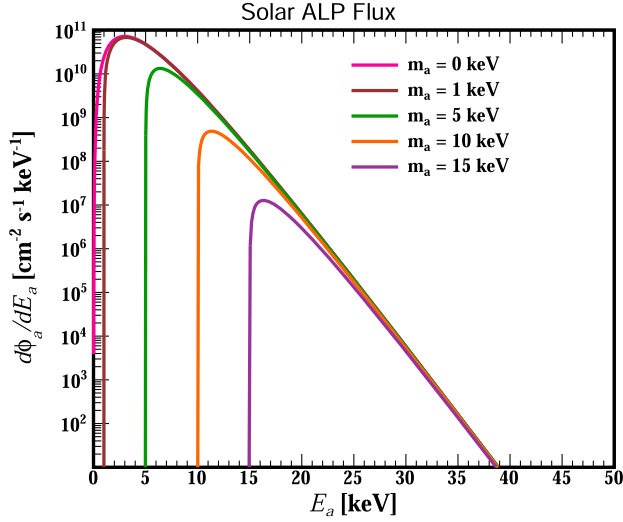
FIG. 6. The differential spectrum for solar-ALPs, following Ref. [37] and taking $g_{a\gamma\gamma} = 10^{-10}$ GeV^{-1} and several m_a as illustration.
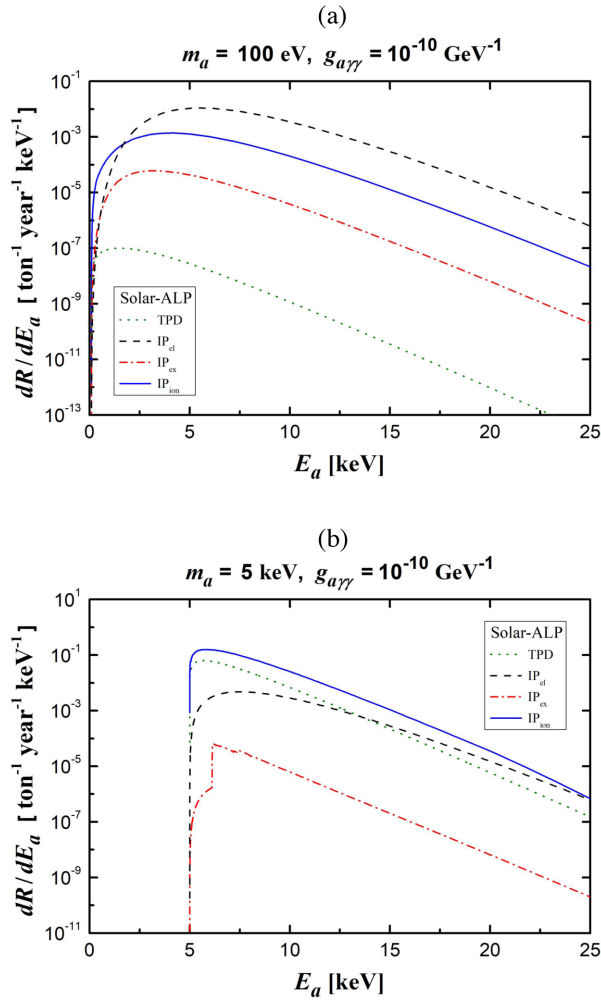

FIG. 7. Differential event rates per ton-year of exposure for solar-ALPs with the four detection channels in liquid xenon, at $g_{a\gamma\gamma} = 10^{-10}$ GeV^{-1} with (a) $m_a = 100$ eV and (b) $m_a = 5$ keV.

TABLE I. Event rates of the four detection channels in liquid xenon for solar- and DM-ALPs, at $g_{a\gamma\gamma} = 10^{-10}$ GeV^{-1}. For IP$_{ex}$, only the dominant final states by electric dipole excitations are included.

| | Event rates (ton^{-1} year^{-1}) | | | |
| | Detection channels | | | |
m_a	TPD	IP$_{el}$	IP$_{ex}$	IP$_{ion}$
	Solar-ALP			
1 meV	$\mathcal{O}(10^{-27})$	6.6×10^{-2}	2.9×10^{-4}	7.8×10^{-3}
1 eV	$\mathcal{O}(10^{-15})$	6.6×10^{-2}	2.9×10^{-4}	7.8×10^{-3}
1 keV	2.8×10^{-3}	6.4×10^{-2}	2.6×10^{-4}	1.3×10^{-2}
5 keV	1.8×10^{-1}	2.4×10^{-2}	9.4×10^{-5}	5.1×10^{-1}
10 keV	8.9×10^{-2}	1.9×10^{-3}	7.8×10^{-5}	3.8×10^{-1}
	DM-ALP			
1 eV	2.5×10^{-4}	$\mathcal{O}(10^{-14})$	0	0
1 keV	250	1.7×10^{-5}	1.6×10^{-3}	500
1 MeV	2.5×10^{8}	9.9×10^{-5}	2.2×10^{-10}	5.0×10^{8}

The total event rates of the four channels at different m_a are presented in Table I. At sub-keV energy (that is, 1 meV, 1 eV, and 1 keV), the IP$_{el}$-rates dominate and show little mass dependence as $v_a \to 1$ in the $E_a \sim$ keV energy range. The subleading contribution is from IP$_{ion}$—still substantial at 10%–20% level. In addition, the $m_a^4/E_a^2 \propto m_a^2$ factor in the transverse response leads to the NR enhancement in Eq. (13) and provides bigger correction at higher m_a. Unlike IP$_{ex}$ which is relatively small and almost mass-independent, the TPD sensitively depends on m_a^4, following Eq. (20). This explains the 12 orders of magnitude increase in the TPD rate when m_a increases from 1 meV to 1 eV and from 1 eV to 1 keV.

2. Solar-ALPs at keV mass (nonrelativistic)

Typical helioscope experiments [41] can place strong bounds on UR solar-ALPs, in particular for $m_a \lesssim 10^{-2}$ eV. The constraints become increasingly weaker in the NR regime as m_a increases, when the coherence wavelength becomes comparable to the detector dimensions. However, ALPs of $m_a \sim$ keV can still be produced in the Sun. Data from experiments on direct DM searches, as we will show in this work, can provide competitive limits from solar-ALPs and complement the ones from helioscopes.

Analytical studies of solar-ALPs cover the entire kinematic regime from NR to relativistic. As a result, the derivations of cross sections and rates are involved and require the incorporation of both atomic longitudinal and transverse responses. The case of $g_{a\gamma\gamma} = 10^{-10}$ GeV^{-1} and $m_a = 5$ keV is considered in Fig. 7(b). The most interesting feature is that IP$_{ion}$ dominates over IP$_{el}$ in the entire energy range, due to the NR enhancement from the transverse response. In addition, since the time dilation effect is not as severe as for the case of sub-keV m_a, the TPD rate is higher than that of IP$_{el}$. The IP$_{ex}$ rate remains

the least significant. The edge structure of IP_{ex} at $E_a = 6.13$ keV is due to the photon double pole when a $2p$-shell electron is excited to a $5d$ or $6s$ orbital, with excitation energy ~ 4.8 keV. The atomic discrete excitations other than the electric-dipole transitions are highly suppressed.

The total event rates for the four detection channels due to NP solar-ALPs at $m_a = 5$ and 10 keV are given in Table I. The IP_{ion} channel dominates the event rates for keV-scale solar-ALPs. The rates would be dramatically suppressed at $m_a > 10$ keV due to the sharp decrease of the solar-ALP fluxes.

B. DM-ALPs

Under the scenario of DM-ALP [5–7], experimental searches for galactic DM can place constraints on the ALP parameter space [10–14]. IP interactions contribute in probing $g_{a\gamma\gamma}$ in direct DM search experiments.

We first derive the event rates and sensitivity regions under the assumption of DM-ALPs and independent of other constraints. We would then study the implications and results in the presence of the DM-ALP cosmological stability bound in Sec. IV C, and conclude what physics information can be obtained from current and future experiments.

The conventional Maxwellian velocity distribution is adopted for the DM-ALP spectrum,

$$f(\vec{v}_a) = \frac{1}{K}\exp\left[-\frac{|\vec{v}_a + \vec{v}_E|^2}{v_0^2}\right]\Theta(v_{esc} - |\vec{v}_a + \vec{v}_E|), \quad (21)$$

where $\vec{v}_a$ is the ALP velocity with respect to Earth and the velocity parameters are $v_0 = 220$ km/s, $v_E = 232$ km/s, and $v_{esc} = 544$ km/s, and K is the normalization factor. The galactic DM density is taken to be $\rho_\chi = 0.3$ GeV/cm^3. After averaging out the seasonal effect, the isotropic differential number density distribution with respect to v_a is

$$\frac{dn_a(v_a)}{dv_a} = \frac{\rho_\chi}{m_a} v_a^2 \int d\Omega_a f(\vec{v}_a), \quad (22)$$

which leads to the DM differential energy spectra,

$$\frac{d\phi_a}{dE_a} = \frac{1}{m_a}\frac{dn(v_a)}{dv_a}. \quad (23)$$

Evaluation of the differential event rates for the three IP and TPD processes follow Eqs. (6) and (20), respectively. DM-ALPs are NR or, equivalently, $\gamma \approx 1$. The TPD rate is therefore not suppressed by time dilation. Since the DM-ALP number density is inversely proportional to m_a, the TPD rate scales only as m_a^2—different from m_a^4 for solar-ALPs. In addition, the flux has no dependence on $g_{a\gamma\gamma}$. The event rates therefore scale as $g_{a\gamma\gamma}^2$.
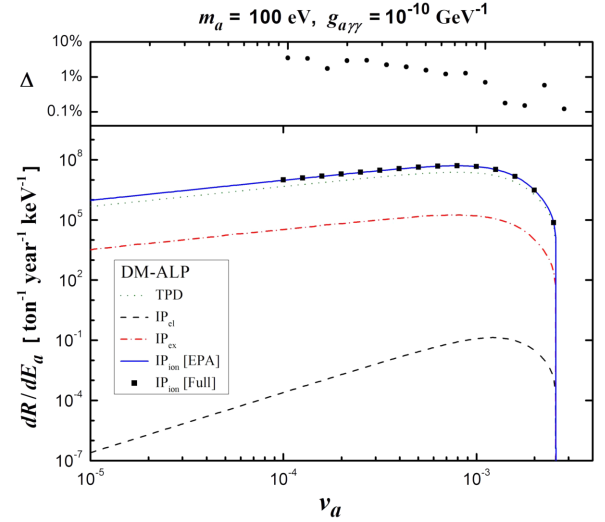

FIG. 8.   Differential event rates per ton-year of exposure for DM-ALPs with the four detection channels in liquid xenon, at $g_{a\gamma\gamma} = 10^{-10}$ GeV^{-1} and $m_a = 100$ eV as illustration. The x axis is in $v_a \simeq \sqrt{2(E_a - m_a)/m_a}$, which is suitable for NR kinematics. The fractional deviation Δ between the Full and EPA calculations of IP_{ion} is shown at the upper panel.

Since DM-ALPs are NR, it can be expected that transverse responses in the IP processes are important due to the double pole of the photon propagator. The differential event rates for the four channels expected at a liquid xenon detector with a ton-year exposure at $g_{a\gamma\gamma} = 10^{-10}$ GeV^{-1} and $m_a = 0.1$ keV (this set of values for m_a and $g_{a\gamma\gamma}$ satisfies the stability requirement) are depicted in Fig. 8. For clarity, the x axis is converted to the DM velocity $v_a \simeq \sqrt{2(E_a - m_a)/m_a}$ with a cutoff at the maximum $v_{esc} + v_E$. Among the three IP channels, IP_{ion} dominates the event rates, while IP_{ex} is subleading. Both are much larger than IP_{el} in which there is no enhancement since the elastic scattering is purely spacelike. In the NR velocity range, the validity of EPA is justified against the full calculations of selected points. The percentage deviations, shown in the upper panel, are less than 3%—consistent with the discussion in Sec. II D and Fig. 5.

We argue in Sec. II C that, as long as the EPA is a valid approximation, the IP_{ion} event rate for NR ALPs in a detector will be twice that of TPD. This is verified in Fig. 8, which implies TPD is as important as IP_{ion} to look for DM-ALPs with a nonzero $g_{a\gamma\gamma}$ coupling. The efficiency aspects of experimentally tagging two photons for the former and one photon plus one electron for the latter will be discussed in Sec. IV.

The total event rates for DM-ALPs at $m_a = 1$ eV, 1 keV, and 1 MeV are given in Table I. At $m_a = 1$ eV, the DM-ALP cannot induce any atomic transitions. Therefore, only IP_{el} is possible. However, the rate is very small compared to that due to a solar-ALP of the same mass because of the limited phase space. On the other hand, the TPD rate is

much bigger than its solar-ALP counterpart because it does not have the extra 10^3 time dilation suppression factor, and the DM-ALP flux is larger than the solar-ALP flux by 8 orders of magnitude. This explains the 11-order difference in their TPD rates.

With m_a at 1 keV and 1 MeV, both IP_{ex} and IP_{ion} are possible and IP_{el} becomes insignificant. As discussed above, IP_{ion} and TPD are the most promising channels for direct detectors, and their rates only differ by a factor of 2. The m_a^2 dependence of IP_{ion} and TPD rates is clearly observed. The rates of IP_{ex} for these two masses suggest some irregularity. This is mostly due to the atomic structure where most discrete excitation energies are in the 10 eV to 10 keV range. At $m_a = 1$ MeV, there is no atomic discrete excitation at ~500 keV $(= m_a/2)$ to match the double pole kinematics, so there is no enhancement for the transverse response. As a result, its rate is even smaller than IP_{el} in which the longitudinal response is larger.

IV. EXPERIMENTAL CONSTRAINTS

A. Selected data

The following datasets are adopted for analysis to derive constraints on the $(m_a, g_{a\gamma\gamma})$ plane:

(1) TEXONO data with (a) point-contact germanium detector at 300 $eV_{ee} - 12$ keV$_{ee}$ [42], and (b) high-purity germanium detector at 12 keV$_{ee}$ to 3000 keV$_{ee}$ [43], selected for having both low threshold and high energy (MeV$_{ee}$) reach with detectors of excellent energy resolution (1.98 keV$_{ee}$ at 1 MeV$_{ee}$) for spectral peak detection.

(2) XENONnT data with liquid xenon at 1–140 keV$_{ee}$ [44,45] selected for its large exposure while having low threshold and background. The background is well-modeled and understood, and is subtracted for ALP searches.

The energy dependence of signal efficiencies in both the TPD and IP_{ion} channels are depicted in Fig. 9. For solar-ALPs which are relativistic, IP_{el} with a one-photon final state is the dominant channel. Signatures are continuous distributions with the ALP spectra convoluted with IP_{el} cross sections. Signal efficiency for single-hit data selection is close to unity at this low (<20 keV$_{ee}$) energy. The DM-ALPs are NR and interact predominantly via the TPD and IP_{ion} channels, the signatures of which are Gaussian peaks at m_a on the total energy depositions over the continuum background spectra. Current DM data focuses on "single-hit" events uncorrelated to veto signals from other detector components. Signal efficiencies of having final-state emissions with full absorption (FA) in the detectors and tagged as single-hit (SH) events have to be evaluated. These differ among the two channels with their different final-states: TPD is with both γ's each having an energy of $E_a/2$; while IP_{ion} has an electron and a photon each at $E_a/2$. In the case of liquid xenon detector, this requirement implies that the
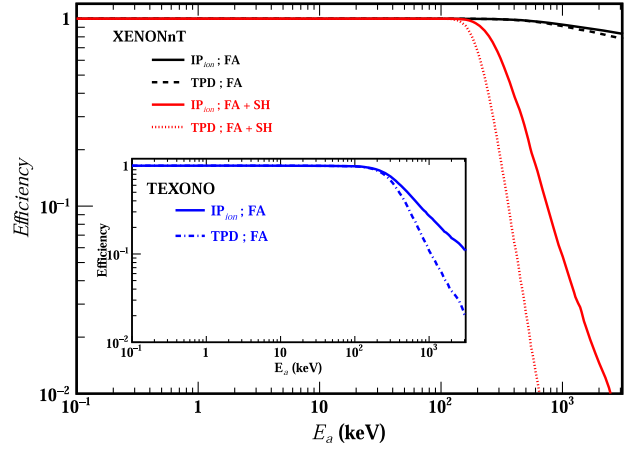

FIG. 9. Signal detection efficiency for DM-ALPs for the leading TPD and IP_{ion} channels as function of E_a in XENONnT [44,45] and TEXONO [42,43] (inset) experiments. Efficiencies due to full absorption (FA) are applicable to both experiments, while single-hit (SH) selection applies in addition to XENONnT. Signatures for solar-ALPs are below 20 keV$_{ee}$, and the efficiency is close to unity.

final states are fully absorbed within a distance corresponding to the spatial resolution ($\sigma_{x,y} = 0.8$ cm and $\sigma_z = 0.3$ cm at 1 MeV$_{ee}$ [45]) away from the vertices.

B. Solar-ALPs

The exclusion regions at 90% confidence level (CL) from the TEXONO and XENONnT data on solar-ALP $g_{a\gamma\gamma}$ are derived. The signal detection efficiencies are 100% as noted. The standalone sensitivity regions are presented in Fig. 10(a). The relevant mass range for solar-ALPs is $m_a < 10^4$ eV, where the blue and red lines represent the constraints from TEXONO and XENONnT, respectively. Also displayed are the upper reaches of the exclusion sensitivity, which are constrained by the solar-ALPs being able to: (a) leave the solar surface, limited by IP_{el} in the Sun (green dotted line), and (b) arrive on Earth, limited by TPD in space (black dotted line).

The leading sensitivities are from the IP_{el} and IP_{ion} channels at the relativistic ($m_a < 1$ keV) and NR ($m_a > 1$ keV) ranges, respectively. Limits derived from XENONnT far exceed that of TEXONO over the entire solar-ALP m_a-range, due to its large exposure and lower background.

The solar-ALP constraints in the global context are illustrated in Fig. 10(b), together with astrophysical and cosmological bounds [11,46–48] as well as predictions from QCD-axion models [49]. The IP_{el} and IP_{ion} channels with solar-ALPs significantly improves on $g_{a\gamma\gamma}$ over the Bragg-scattering constraints from CDMS [19] and EDELWEISS [20]. It also extends the detectable window in m_a from 1 eV to $\mathcal{O}(10$ keV) beyond the reach of the CAST helioscope experiment [41].

(a)

Solar - ALP
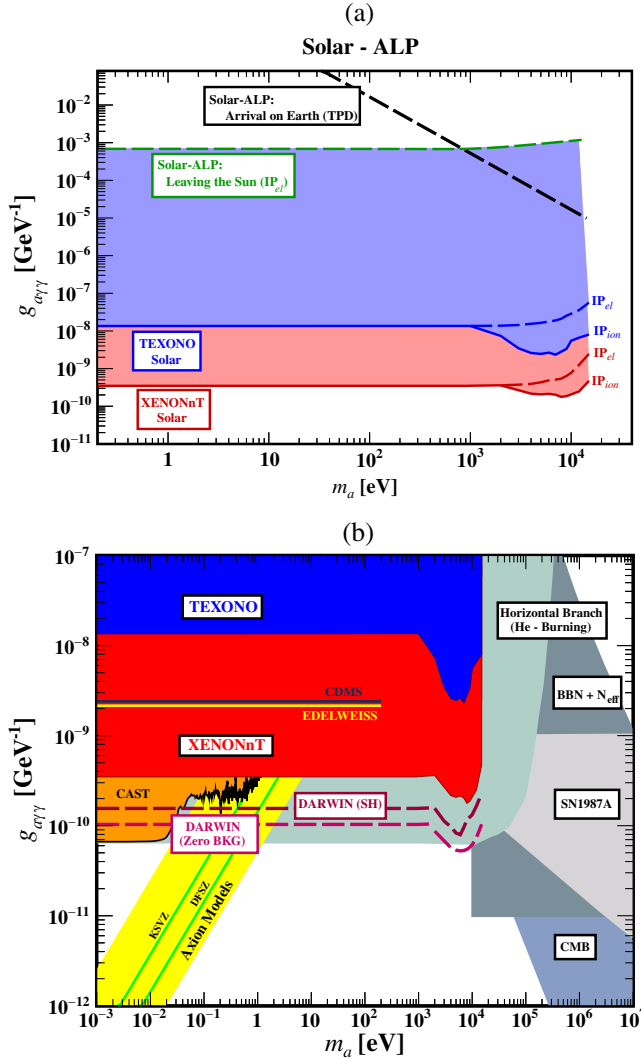

(a)

DM - ALP

(b)

(b)

FIG. 10.   (a) Standalone sensitivity regions at 90% CL in $(m_a, g_{a\gamma\gamma})$ from the TEXONO [42,43] and XENONnT [44,45] experiments with solar-ALPs. Contributions from the leading channels of IP_{el} and IP_{ion} are displayed. Upper reaches of the sensitivity regions due to survival from the Sun is shown. (b) Exclusion plot in $(m_a, g_{a\gamma\gamma})$ at 90% CL, showing the solar-ALP limits from TEXONO and XENONnT experiments. The astrophysical and cosmological bounds [11,46–48] are the light shaded regions. The predicted band for QCD axions [49] is in yellow. Superimposed are the current constraints from solar-ALPs with Bragg scattering [19,20] and helioscope [41] experiments, as well as the sensitivity reaches of the DARWIN project [50] at standard SH-selection and zero-background scenarios.

C. DM-ALPs

With the detection efficiencies of Fig. 9 taken into account, the standalone sensitivity regions for DM-ALPs analysis independent of other processes are derived. The probed parameter space at 90% CL of the leading channels TPD and IP_{ion} for DM-ALPs by the TEXONO and XENONnT data are presented by the blue and red regions, respectively, in Fig. 11(a). The relevant mass range for
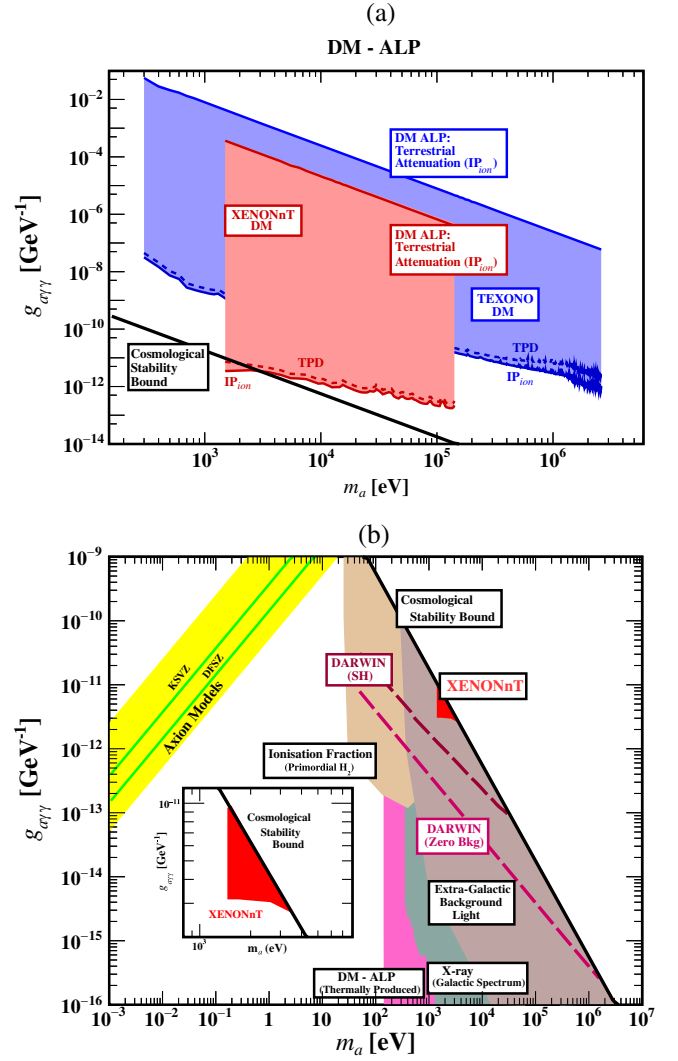
FIG. 11.   (a) Standalone sensitivity regions at 90% CL in $(m_a, g_{a\gamma\gamma})$ from the TEXONO [42,43] and XENONnT [44,45] experiments with DM-ALPs. Contributions from the leading channels of IP_{ion} and TPD are displayed. Upper reaches of the sensitivity regions due to survival of terrestrial attenuation effects are shown. The cosmological stability bound [46,51,52] is denoted by the bold black line. (b) Exclusion plot in $(m_a, g_{a\gamma\gamma})$ at 90% CL, which results from the scenario of DM-ALPs. The stability bound (black) dictates that only a small region (red) is excluded by XENONnT [44,45]. The astrophysical and cosmological constraints [11,52], which are consequences of DM-ALPs, are included. The predictions from QCD axions [49] are displayed as the yellow band. Superimposed are the sensitivity reaches of the DARWIN project [50] at standard SH-selection and zero-background scenarios, indicating that a new detection window is opened and substantial region can be probed.

DM-ALPs is 10^4 eV $\leq m_a \leq 10^7$ eV, corresponding to the measurement dynamic range of the experiments. The upper reaches of the sensitivity regions are bounded by terrestrial attenuation by the Earth and its atmosphere before the DM-ALPs can reach the detectors. XENONnT provides
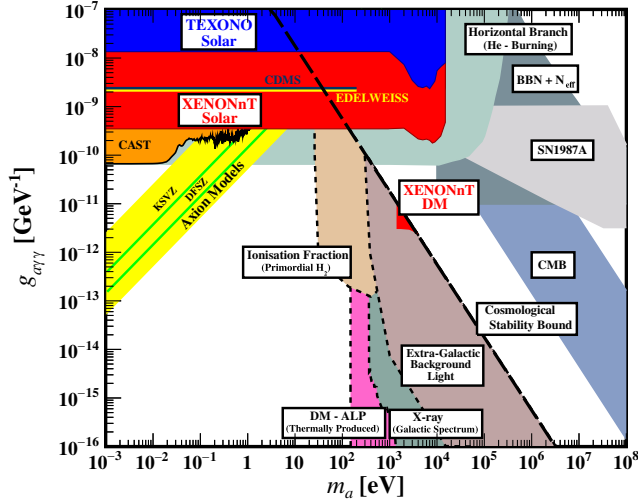
FIG. 12. Summary plot of existing constraints on $g_{a\gamma\gamma}$ versus m_a in ALPs. Those in dotted lines only apply under the assumption that ALPs are the cosmological DM [52]. The yellow band are predictions from QCD axion models [49].

better sensitivities, at $m_a \sim$ 1–100 keV. TEXONO, being a surface experiment with larger dynamic range, is sensitive to higher $g_{a\gamma\gamma}$ and can explore an extended mass range of $m_a \sim$ 300 eV–3 MeV.

However, it is necessary to place this projected stand-alone sensitivity in relation to other astrophysical and cosmological constraints. The decay of ALPs with $m_a <$ 1 MeV to e^+e^- via g_{aee} is not allowed by kinematics, but ALPs of any mass can have TPD via $g_{a\gamma\gamma}$. This places severe requirement on ALP stability—the TPD lifetime ($1/\Gamma^V_{a\gamma\gamma}$) has to be longer than the age of the Universe [46,51,52] in order for the DM-ALP to reach and be observable in terrestrial experiments. This implies part of the $(m_a, g_{a\gamma\gamma})$ parameter space is not accessible by the direct experimental searches of DM-ALPs. As an illustration, the case of $m_a = 1$ keV, $g_{a\gamma\gamma} \gtrsim 2 \times 10^{-11}$ GeV^{-1} is not viable. The DM-ALPs would not reach the detectors and no physics information can be extracted.[2]

A summary of experimental constraints on $g_{a\gamma\gamma}$ from DM-ALPs together with predictions from QCD-axion models [49] are presented in Fig. 11(b). The TPD stability bound is marked as the bold black line. The IP$_{ion}$ channel opens a large unexplored detection window for DM-ALPs. The current sensitivities, however, do not yet match those required by the stability bound, and no physics constraints can be placed. A notable crack is at a small corner at $m_a \sim 10^3$ eV, where the sensitivity from XENONnT data [44,45] exceeds that of stability bound, so that the parameter space in red is probed and excluded. Other astrophysical and

cosmological bounds under the DM-ALP scenario [11,52] are also included in Fig. 11(b). The constraints are valid only at regions where $g_{a\gamma\gamma}$ is weak enough to survive the cosmological stability bound.

V. SUMMARY AND PROSPECTS

In this work, we explored new detection channels to probe $g_{a\gamma\gamma}$ with terrestrial experiments, opening up a large parameter space in $(m_a, g_{a\gamma\gamma})$ for laboratory-based experimental searches of solar-ALPs and DM-ALPs. Both results are combined into the summary plot of Fig. 12. The constraints in dotted lines represent those which only apply under the assumption that ALPs are the cosmological DM and are stable relative to the age of the Universe. Though the astrophysical and cosmological constraints are in general more stringent than the laboratory limits, they usually have strong model and parameter dependence. For instance, the "DM-ALP (thermally produced)" constraint assumes thermal production of DM-ALP in the early Universe such that its density cannot exceed that implied by the DM relic abundance [46]. This bound would be completely evaded under DM-ALP production scenarios with nonthermal processes [52].

Experimentally, the IP$_{ion}$ channel with NR ALPs offers a very distinct signature: an electron and a photon with equal energy originated from a common vertex. This feature can be used for further background suppression while retaining good signal efficiency. The projected sensitivities of the next generation liquid xenon project DARWIN [50] at 200 ton-year exposure and 50 eV$_{ee}$ threshold are superimposed in Figs. 10(b) and 11(b), showing one with typical single-hit selection with the projected background subtracted, and another with an idealized zero-background all-multiplicity full-efficiency measurement. In particular, Fig. 11(b) indicates that the IP$_{ion}$ sensitivities of future projects would exceed the cosmological stability bound for DM-ALPs. A new detection window would be opened by the IP processes, and an unexplored parameter space can be studied.

Recent works [53,54] identify that g_{aee} coupling at the quantum one-loop level can produce experimental signatures that resemble those from $g_{a\gamma\gamma}$ interactions. Accordingly, experimental constraints such as those from IP effects of this work can be translated to bounds on g_{aee}. This will be one of the themes for our future research efforts.

ACKNOWLEDGMENTS

---

[2]The relatively-long-lived ALPs can be studied by other means such as in colliders and from probes of the early Universe.

[1] R. D. Peccei and H. R. Quinn, *CP* Conservation in the Presence of Pseudoparticles, Phys. Rev. Lett. **38,** 1440 (1977).

[2] R. D. Peccei and H. R. Quinn, Constraints imposed by *CP* conservation in the presence of pseudoparticles, Phys. Rev. D **16,** 1791 (1977).

[3] S. Weinberg, A New Light Boson?, Phys. Rev. Lett. **40,** 223 (1978).

[4] F. Wilczek, Problem of Strong *P* and *T* Invariance in the Presence of Instantons, Phys. Rev. Lett. **40,** 279 (1978).

[5] J. Preskill, M. B. Wise, and F. Wilczek, Cosmology of the invisible axion, Phys. Lett. **120B,** 127 (1983).

[6] L. Abbott and P. Sikivie, A cosmological bound on the invisible axion, Phys. Lett. **120B,** 133 (1983).

[7] M. Dine and W. Fischler, The not-so-harmless axion, Phys. Lett. **120B,** 137 (1983).

[8] G. Raffelt and L. Stodolsky, New particles from nuclear reactions in the sun, Phys. Lett. **119B,** 323 (1982).

[9] R. Cameron *et al.*, Search for nearly massless, weakly coupled particles by optical techniques, Phys. Rev. D **47,** 3707 (1993).

[10] P. W. Graham, I. G. Irastorza, S. K. Lamoreaux, A. Lindner, and K. A. van Bibber, Experimental searches for the axion and axion-like particles, Annu. Rev. Nucl. Part. Sci. **65,** 485 (2015).

[11] I. G. Irastorza and J. Redondo, New experimental approaches in the search for axion-like particles, Prog. Part. Nucl. Phys. **102,** 89 (2018).

[12] P. Sikivie, Invisible axion search methods, Rev. Mod. Phys. **93,** 015004 (2021).

[13] K. Choi, S. H. Im, and C. Sub Shin, Recent progress in the physics of axions and axion-like particles, Annu. Rev. Nucl. Part. Sci. **71,** 225 (2021).

[14] R. L. Workman *et al.* (Particle Data Group), Review of particle physics, Prog. Theor. Exp. Phys. **2022,** 083C01 (2022).

[15] C. O'Hare, cajohare/axionlimits: Axionlimits, https:// cajohare.github.io/AxionLimits/ (2020).

[16] F. T. Avignone III, D. Abriola, R. L. Brodzinski, J. I. Collar, R. J. Creswick, D. E. DiGregorio, H. A. Farach, A. O. Gattone, C. K. Guérard, F. Hasenbalg, H. Huck, H. S. Miley, A. Morales, J. Morales, S. Nussinov, A. Ortiz de Solórzano, J. H. Reeves, J. A. Villar, and K. Zioutas (SOLAX Collaboration), Experimental Search for Solar Axions via Coherent Primakoff Conversion in a Germanium Spectrometer, Phys. Rev. Lett. **81,** 5068 (1998).

[17] R. Bernabei *et al.*, Search for solar axions by Primakoff effect in NaI crystals, Phys. Lett. B **515,** 6 (2001).

[18] A. Morales *et al.* (COSME Collaboration), Particle dark matter and solar axion searches with a small germanium detector at the Canfranc Underground Laboratory, Astropart. Phys. **16,** 325 (2002).

[19] Z. Ahmed *et al.* (CDMS Collaboration), Search for Axions with the CDMS Experiment, Phys. Rev. Lett. **103,** 141802 (2009).

[20] E. Armengaud *et al.*, Axion searches with the EDELWEISS-II experiment, J. Cosmol. Astropart. Phys. 11 (2013) 067.

[21] S. Barshay, H. Faissner, R. Rodenberg, and H. De Witt, Coherent Conversion of Very Light Pseudoscalar Bosons, Phys. Rev. Lett. **46,** 1361 (1981).

[22] F. T. Avignone III, C. Baktash, W. C. Barker, F. P. Calaprice, R. W. Dunford, W. C. Haxton, D. Kahana, R. T. Kouzes, H. S. Miley, and D. M. Moltz, Search for axions from the 1115-keV transition of ^{65}Cu, Phys. Rev. D **37,** 618 (1988).

[23] W. Buchmuller and F. Hoogeveen, Coherent production of light scalar particles in Bragg scattering, Phys. Lett. B **237,** 278 (1990).

[24] E. A. Paschos and K. Zioutas, A proposal for solar axion detection via Bragg scattering, Phys. Lett. B **323,** 367 (1994).

[25] R. J. Creswick, F. T. Avignone III, H. A. Farach, J. I. Collar, A. O. Gattone, S. Nussinov, and K. Zioutas, Theory for the direct detection of solar axions by coherent Primakoff conversion in germanium detectors, Phys. Lett. B **427,** 235 (1998).

[26] J. B. Dent, B. Dutta, J. L. Newstead, and A. Thompson, Inverse Primakoff Scattering as a Probe of Solar Axions at Liquid Xenon Direct Detection Experiments, Phys. Rev. Lett. **125,** 131805 (2020).

[27] C. Gao, J. Liu, L.-T. Wang, X.-P. Wang, W. Xue, and Y.-M. Zhong, Reexamining the Solar Axion Explanation for the XENON1T Excess, Phys. Rev. Lett. **125,** 131806 (2020).

[28] T. Abe, K. Hamaguchi, and N. Nagata, Atomic form factors and inverse Primakoff scattering of axion, Phys. Lett. B **815,** 136174 (2021).

[29] J.-W. Chen, H.-C. Chi, K.-N. Huang, C.-P. Liu, H.-T. Shiao, L. Singh, H. T. Wong, C.-L. Wu, and C.-P. Wu, Atomic ionization of germanium by neutrinos from an *ab initio* approach, Phys. Lett. B **731,** 159 (2014).

[30] J.-W. Chen, H.-C. Chi, H.-B. Li, C.-P. Liu, L. Singh, H. T. Wong, C.-L. Wu, and C.-P. Wu, Constraints on millicharged neutrinos via analysis of data from atomic ionizations with germanium detectors at sub-keV sensitivities, Phys. Rev. D **90,** 011301 (2014).

[31] J.-W. Chen, H.-C. Chi, K.-N. Huang, H.-B. Li, C.-P. Liu, L. Singh, H. T. Wong, C.-L. Wu, and C.-P. Wu, Constraining

neutrino electromagnetic properties by germanium detectors, Phys. Rev. D **91**, 013005 (2015).

[32] M. K. Pandey, L. Singh, C.-P. Wu, J.-W. Chen, H.-C. Chi, C.-C. Hsieh, C.-P. Liu, and H. T. Wong, Constraints from a many-body method on spin-independent dark matter scattering off electrons using data from germanium and xenon detectors, Phys. Rev. D **102**, 123025 (2020).

[33] C.-P. Liu, C.-P. Wu, J.-W. Chen, H.-C. Chi, M. K. Pandey, L. Singh, and H. T. Wong, Spin-dependent dark matter-electron interactions, Phys. Rev. D **106**, 063003 (2022).

[34] M. C. D. Marsh, The darkness of spin-0 dark radiation, J. Cosmol. Astropart. Phys. 01 (2015) 017.

[35] J.-W. Chen, H.-C. Chi, S.-T. Lin, C.-P. Liu, L. Singh, H. T. Wong, C.-L. Wu, and C.-P. Wu, Atomic ionization by sterile-to-active neutrino conversion and constraints on dark matter sterile neutrinos with germanium detectors, Phys. Rev. D **93**, 093012 (2016).

[36] S. Andriamonje et al. (CAST Collaboration), An improved limit on the axion-photon coupling from the CAST experiment, J. Cosmol. Astropart. Phys. 04 (2007) 010.

[37] L. Di Lella, A. Pilaftsis, G. Raffelt, and K. Zioutas, Search for solar Kaluza-Klein axions in theories of low-scale quantum gravity, Phys. Rev. D **62**, 125011 (2000).

[38] G. G. Raffelt, Plasmon decay into low-mass bosons in stars, Phys. Rev. D **37**, 1356 (1988).

[39] G. G. Raffelt, Astrophysical axion bounds diminished by screening effects, Phys. Rev. D **33**, 897 (1986).

[40] J. N. Bahcall, A. M. Serenelli, and S. Basu, New solar opacities, abundances, helioseismology, and neutrino fluxes, Astrophys. J. **621**, L85 (2005).

[41] CAST Collaboration, New CAST limit on the axion-photon interaction, Nat. Phys. **13**, 584 (2017).

[42] L. Singh et al. (TEXONO Collaboration), Constraints on millicharged particles with low threshold germanium detectors at Kuo-Sheng Reactor Neutrino Laboratory, Phys. Rev. D **99**, 032009 (2019).

[43] H. T. Wong et al. (TEXONO Collaboration), A search of neutrino magnetic moments with a high-purity germanium detector at the Kuo-Sheng nuclear power station, Phys. Rev. D **75**, 012001 (2007).

[44] E. Aprile et al. (XENON Collaboration), Search for New Physics in Electronic Recoil Data from XENONnT, Phys. Rev. Lett. **129**, 161805 (2022).

[45] E. Aprile et al. (XENON Collaboration), XENON1T dark matter data analysis: Signal reconstruction, calibration and event selection, Phys. Rev. D **100**, 052014 (2019).

[46] D. Cadamuro and J. Redondo, Cosmological bounds on pseudo Nambu-Goldstone bosons, J. Cosmol. Astropart. Phys. 02 (2012) 032.

[47] J. Jaeckel, P. C. Malta, and J. Redondo, Decay photons from the axionlike particles burst of type II supernovae, Phys. Rev. D **98**, 055032 (2018).

[48] P. F. Depta, M. Hufnagel, and K. Schmidt-Hoberg, Robust cosmological constraints on axion-like particles, J. Cosmol. Astropart. Phys. 05 (2020) 009.

[49] G. G. Raffelt, Axions: Motivation, limits and searches, J. Phys. A **40**, 6607 (2007).

[50] J. Aalbers et al. (DARWIN Collaboration), DARWIN: Towards the ultimate dark matter detector, J. Cosmol. Astropart. Phys. 11 (2016) 017.

[51] E. Masso and R. Toldra, Light spinless particle coupled to photons, Phys. Rev. D **52**, 1755 (1995).

[52] P. Arias, D. Cadamuro, M. Goodsell, J. Jaeckel, J. Redondo, and A. Ringwald, WISPy cold dark matter, J. Cosmol. Astropart. Phys. 06 (2012) 013.

[53] R. Z. Ferreira, M. C. D. Marsh, and E. Müller, Do Direct Detection Experiments Constrain Axionlike Particles Coupled to Electrons?, Phys. Rev. Lett. **128**, 221302 (2022).

[54] R. Z. Ferreira, M. D. Marsh, and E. Müller, Strong supernovae bounds on ALPs from quantum loops, J. Cosmol. Astropart. Phys. 11 (2022) 057.